



## Tunable Nano-Interfaces between MnO<sub>x</sub> and Layered Double Hydroxides Boost Oxygen Evolving Electrocatalysis

Journal:	<i>Journal of Materials Chemistry A</i>
Manuscript ID	TA-COM-08-2018-007508.R1
Article Type:	Communication
Date Submitted by the Author:	30-Aug-2018
Complete List of Authors:	Xue, Yudong; Yale University, Department of Chemical and Environmental Engineering Fishman, Zachary; Yale University, Chemical Engineering Rohr, Jason; Yale University, Chemistry Pan, Zhenhua; Yale University, Wang, Yunting; China University of Mining and Technology (Beijing) Zhang, Chunhui; China University of Mining & Technology (Beijing), Zheng, Shili; National Engineering Laboratory for Hydrometallurgical Cleaner Production Technology, Key Laboratory of Green Process and Engineering, Institute of Process Engineering, Chinese Academy of Sciences, 1 North 2nd Street, Zhongguancun, Haidian District, Beijing, 100190, People's Republic of China Zhang, Yi; a. National Engineering Laboratory for Hydrometallurgical Cleaner Production Technology, Key Laboratory of Green Process and Engineering, Institute of Process Engineering, Chinese Academy of Sciences Hu, Shu; Yale University,

# Tunable Nano-Interfaces between MnO<sub>x</sub> and Layered Double Hydroxides Boost Oxygen Evolving Electrocatalysis

Yudong Xue,<sup>a,b,c,d</sup> Zachary S. Fishman,<sup>a,c</sup> Jason A. Röhr,<sup>a,c</sup> Zhenhua Pan,<sup>a,c</sup> Yunting Wang,<sup>e</sup> Chunhui Zhang,<sup>e</sup> Shili Zheng,<sup>b\*</sup> Yi Zhang<sup>b</sup> and Shu Hu,<sup>a,c\*</sup>

<sup>a</sup> *Department of Chemical and Environmental Engineering, Yale University, New Haven, Connecticut 06511, United States.*

<sup>b</sup> *National Engineering Laboratory for Hydrometallurgical Cleaner Production Technology, Key Laboratory of Green Process and Engineering, Institute of Process Engineering, Chinese Academy of Sciences, Beijing 100190, China.*

<sup>c</sup> *Energy Sciences Institute, Yale University, West Haven, Connecticut 06516, United States.*

<sup>d</sup> *University of Chinese Academy of Sciences, Beijing 100049, China.*

<sup>e</sup> *School of Chemical and Environmental Engineering, China University of Mining and Technology (Beijing), Beijing 100083, China.*

*Corresponding author: Shu Hu, e-mail: shu.hu@yale.edu, Tel: +1-203-737-6521; Shili Zheng, e-mail: slzheng@ipe.ac.cn, Tel: +86 10 82544858*

**Abstract:**

Development of low overpotential, non-precious metal oxide electrocatalysts is important for the sustainable water oxidation using renewable energy. Here we report the fabrication of nano-interfaces between  $\text{MnO}_x$  nanoscale islands and NiFe layered double hydroxide (LDH) nanosheets, which were chosen as baseline electrocatalysts for OER activity tuning. The  $\text{MnO}_x$  nano-islands were grown on surfaces of NiFe-LDH nanosheets by atomic layer deposition (ALD). Morphology and structural characterizations indicated that the  $\text{MnO}_x$  formed nanoscale flat islands which uniformly covered the surfaces of NiFe-LDH nanosheets, giving rise to a large density of three-dimensional nano-interface at the NiFe-LDH/ $\text{MnO}_x$ /electrolyte multi-phase boundaries. We showed by x-ray spectroscopic characterizations that these nano-interfaces induced electronic interactions between NiFe-LDH nanosheets and  $\text{MnO}_x$  nano-islands. Through such modification, the Fermi level of original NiFe-LDH was lowered by electron donation to  $\text{MnO}_x$  nano-islands, dramatically boosting the OER performance of these electron-deficient NiFe-LDH catalysts. Using only 10-cycle of ALD  $\text{MnO}_x$ , the  $\text{MnO}_x$ /NiFe-LDH nanocomposites exhibited remarkable and enhanced electrocatalytic activity of 174 mV overpotentials at  $10 \text{ mA cm}^{-2}$ . This work demonstrates a promising pathway for tuning the transition metal electrocatalysts via a genetic ALD surface modification technique.

**Keywords:** atomic layer deposition, oxygen evolution reaction, layered double hydroxides, manganese oxide, electrocatalysis

**1. Introduction**

Currently, the interest in electrochemical oxygen evolution is growing for the applications of efficient and sustainable energy conversion and storage, such as water splitting and metal-air batteries.<sup>1-6</sup> Oxygen evolution reaction (OER) concerns electrical or photo-driven oxidation of water for producing molecular oxygen, which has been a major bottleneck for overall water splitting to generate H<sub>2</sub> fuels from sustainable energy sources.<sup>7</sup> The required overpotential at a given operating current density usually exceeds that for H<sub>2</sub> evolution.<sup>8-11</sup> Among the most efficient OER catalysts, precious metal oxides such as RuO<sub>2</sub> and IrO<sub>2</sub> suffer from elemental scarcity and high cost.<sup>12</sup> Alternatively, NiFe-based layered double hydroxides (LDH), a typical two-dimensional nanomaterial, exhibit outstanding OER activity compared to other mixed metal oxides, metal hydroxides, perovskites and noble metals in base.<sup>13-15</sup> Gong et al. decorated NiFe-LDH on carbon nanotube surfaces and achieved faster electron transfer rates and enhanced OER activity.<sup>16</sup> Zhou et al. introduced reducing flame treatments to NiFe-LDH surfaces for improving their OER performance by creating abundant surface oxygen vacancies.<sup>17</sup> However, those oxygen vacancies will likely annihilate during long-term operation of electrocatalysts, especially under anodic conditions. Importantly, such surface modification is considered as an emerging strategy for catalyst tuning to further improve the record activity of NiFe-LDH OER catalysts.<sup>18</sup>

In nature photosynthesis, manganese plays a vital role for the oxygen evolution in biological systems.<sup>19</sup> Nature uses three-dimensional structures of cubic Mn-O-Ca centres for oxygen evolution, whereas the structures of synthetic water-oxidation catalysts reported so far were mostly two dimensional such as inorganic NiFe-LDH sheets or divalent metal centres with an oxo-bridge, but their active sites are not yet three-

dimensional (3D).<sup>20</sup> Numerous studies have reported that manganese oxides including MnO, MnO<sub>2</sub>, and Mn<sub>2</sub>O<sub>3</sub> are effective OER catalysts.<sup>21, 22</sup> MnO<sub>x</sub> is susceptible to changing its surface oxidation state, which is beneficial for accepting or donating electrons during electrocatalysis.<sup>23</sup>

These previous works have motivated the atomic precision surface tuning by anchoring nanoscale MnO<sub>x</sub> composites over two-dimensional NiFe-LDH nanosheets, to achieve three-dimensional (3D) active sites formed onto the LDH catalysts. However, traditional deposition methods for MnO<sub>x</sub>, such as electrodeposition,<sup>24</sup> spray deposition,<sup>25</sup> and thermal decomposition<sup>26</sup> have difficulties in achieving deposition at the level of atomic precision. It is very difficult for these synthesis processes to fine tune the 3D structures of catalyst active sites and to achieve conformality over nano-structured catalysts. For example, Jin *et al.* reported superior catalytic performance of sub-10 nm-sized MnO<sub>x</sub> nanocrystals that are monodispersed, partially oxidized, and fabricated by thermal decomposition, but it is difficult to precisely control their sizes at the nanometer or sub-nanometer level.<sup>26</sup> Besides, electrodeposited MnO<sub>2</sub> was reported as a stable OER catalyst, but electrodeposition cannot easily achieve atomic scale deposition and tunability.<sup>25</sup>

Atomic layer deposition (ALD), owing to the capability of atomically precise control via surface-limited chemical growth, has attracted great attention for modifying surfaces and improving the performance durability in broad applications including (photo-)catalysis, photovoltaics, and batteries.<sup>27, 28</sup> Most reports about ALD oxide coatings were focused on corrosion protection or stabilization for water splitting (especially photoanodes).<sup>29-33</sup> As for tuning the electrocatalytic performance, constructing

catalytically active sites by surface modification using ALD metal oxides is still less investigated.

Herein, we have designed and fabricated OER electrocatalysts of  $\text{MnO}_x/\text{NiFe-LDH}$  nanocomposites by ALD  $\text{MnO}_x$  growth over NiFe-LDH nanosheets that were synthesized and immobilized onto Ni foams as conductive supports. The ALD-modified catalyst nanocomposites exhibited superb OER activity because of chemical bonding and atomic-scale anchoring of  $\text{MnO}_x$  nano-islands onto the nanosheet surfaces. Their crystal structures, surface morphology, elemental distribution, and oxidation states were systematically characterized using X-ray diffraction (XRD), scanning electron microscope (SEM), transmission electron microscopy (TEM), energy dispersive X-ray spectroscopy (EDX), and X-ray photoelectron spectroscopy (XPS). Enhanced OER catalytic activity was observed and was attributed to the newly created 3D nano-interfaces at  $\text{MnO}_x/\text{NiFe-LDH}$  nanocomposites, which promise a new class of practical energy conversion materials.

## 2. Experimental Synthesis and Characterization

$\text{Fe}(\text{NO}_3)_3 \cdot 9\text{H}_2\text{O}$  (99.99%),  $\text{Ni}(\text{NO}_3)_2 \cdot 6\text{H}_2\text{O}$  (99%),  $\text{Mn}(\text{NO}_3)_2 \cdot 4\text{H}_2\text{O}$  (99%), and  $\text{CO}(\text{NH}_2)_2$  (99.8%) were purchased from Sigma-Aldrich and were used as-received. Ni foam (99.8%, 1.5 mm thick) plates were purchased from Taiyuan Lizhiyuan Battery. Fluorine-doped tin oxide (FTO) substrates (TEC15) were purchased from Hartford Glass Co. All solutions were prepared using deionized water (18  $\text{M}\Omega \cdot \text{cm}$ ) obtained from a Millipore deionized water system. The NiFe-LDH nanosheets were synthesized using a hydrothermal method and were directly deposited onto Ni foam plates during synthesis.

0.5 mmol  $\text{Ni}(\text{NO}_3)_2 \cdot 6\text{H}_2\text{O}$ , 0.5 mmol  $\text{Fe}(\text{NO}_3)_3 \cdot 9\text{H}_2\text{O}$ , and 5 mmol  $\text{CO}(\text{NH}_2)_2$  were dissolved in 30 mL water. Ni foam was first cut into pieces at a size of  $1 \text{ cm} \times 1.5 \text{ cm}$ , and then subsequently cleaned with concentrated HCl (37% w/w), water, and ethanol with each step for 5 min. The Ni foam was immediately transferred to a 50-mL autoclave which was maintained at  $130 \text{ }^\circ\text{C}$  for 12h. After cooling to room temperatures, the electrode was washed with water and ethanol and subsequently dried in vacuum at  $60 \text{ }^\circ\text{C}$  for 4 h. Following this procedure, NiFe-LDH nanosheets were uniformly grown on the Ni foam and inside its pores.

In order to construct  $\text{MnO}_x/\text{LDH}$  nano-interfaces and investigate their activity enhancement,  $\text{MnO}_x$  was deposited onto the LDH/Ni foam substrates by ALD from the top surface side. ALD growth of  $\text{MnO}_x$  was performed using an Ultratech Fiji G2a ALD system. Bis-(ethylcyclopentadienyl)manganese ( $\text{Mn}(\text{EtCp})_2$ , Strem Chemicals, 98%) was used as Mn precursor. The ALD chamber was set at  $150 \text{ }^\circ\text{C}$  during the growth. One  $\text{MnO}_x$  deposition cycle consisted of a 0.06 s pulse of  $\text{H}_2\text{O}$ , 15 s pause, followed by two 0.25 s pulses of  $\text{Mn}(\text{EtCp})_2$  (the precursor temperature held at  $100 \text{ }^\circ\text{C}$ ) spaced 7 s apart, and completed with another 0.06 s pulse of  $\text{H}_2\text{O}$ .<sup>34,35</sup> The total number of cycles varied at 5, 10, 20, and 50 cycles, which was adjusted to target a series of coverage for  $\text{MnO}_x$  modification. The FTO was also used as a  $\text{MnO}_x$  growth substrate for XPS characterization. For comparison, NiFeMn-LDH electrocatalysts were synthesized with a similar hydrothermal procedure as the NiFe-LDH synthesis by using 0.4 mmol  $\text{Ni}(\text{NO}_3)_2 \cdot 6\text{H}_2\text{O}$ , 0.4 mmol  $\text{Fe}(\text{NO}_3)_3 \cdot 9\text{H}_2\text{O}$ , 0.1 mmol  $\text{Mn}(\text{NO}_3)_2 \cdot 4\text{H}_2\text{O}$ , and 5 mmol  $\text{CO}(\text{NH}_2)_2$  as the precursors.

The electrochemical measurements were carried out using a Bio-Logic S200 potentiostat in a three-electrode cell. Cyclic voltammetry (CV) and linear sweep voltammetry (LSV), with a scan rate of  $1 \text{ mV s}^{-1}$ , were taken in a  $1 \text{ M KOH (aq)}$  electrolyte. A carbon rod and a Hg/HgO electrode were used as the counter electrode and the reference electrode, respectively. The standard deviations of overpotentials were calculated by testing the electrodes for 5 times. Electrochemical impedance spectroscopy (EIS) was measured in the same cell at an overpotential of  $300 \text{ mV}$  from  $10^5$  to  $10^{-1} \text{ Hz}$ . The stability test was carried out using a chronopotentiometry technique at a current density of  $10 \text{ mA cm}^{-2}$ . A Hitachi SU8230 UHR Cold field emission SEM and a FEI Tecnai Osiris TEM were used for studying the surface morphology and elemental distribution. The XPS measurements were performed using a PHI Versa Probe II Scanning XPS Microprobe equipped with a monochromated Al source. The obtained data were analyzed using the XPS Peak software. XRD patterns were collected from a Rigaku SmartLab X-Ray diffractometer by using a  $\text{Cu K}\alpha$  source. The Faradaic efficiency of oxygen evolution on the  $\text{MnO}_x/\text{LDH}/\text{Ni}$  foam electrodes was quantified by comparing the amount of oxygen to that on a standard Ir electrode.<sup>34</sup> The concentration of oxygen was measured by an oxygen probe (OX-NP, Unisense). The TOF value was calculated as follows:

$$\text{TOF} = \frac{jS}{4nF} \quad (1)$$

Where  $j$  is measured current density,  $S$  is the geometric area of electrode,  $n$  is the moles of active materials deposited on the working electrode based on the moles of all metal species,  $F$  is the Faradic constant ( $96485 \text{ C mol}^{-1}$ ).<sup>36,37</sup> The metal ratio of LDH on Ni foam was determined based on inductively coupled plasma-mass spectrometry (ICP-



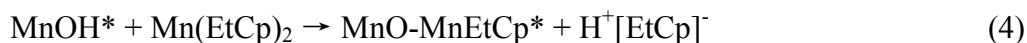
MS, Model iCAP Qc, Thermo Scientific) by exfoliating the LDH nanomaterials from the electrode carefully. The moles of active materials on the Ni foam was calculated by the Fe molar amount and the Ni/Fe ratio.

### 3. Results and Discussion

To test electrocatalytic behaviour, the 3D MnO<sub>x</sub>/NiFe-LDH nanocomposite electrode was prepared via a two-step “bottom-up” approach consisting of a hydrothermal synthesis process and a subsequent ALD modification process. Specifically, the NiFe-LDH nanosheet arrays were first grown on a Ni foam substrate and then decorated with nano-islands of MnO<sub>x</sub> by ALD synthesis. MnO<sub>x</sub> was chemically grown on NiFe-LDH surfaces by using Mn(EtCp)<sub>2</sub> as the Mn precursor and H<sub>2</sub>O as the co-reactant. Figs. S1 and S2 illustrates the ALD process consisting of successive self-limiting surface reactions between the precursor (Mn(EtCp)<sub>2</sub>) vapors and H<sub>2</sub>O over the NiFe-LDH substrate. At the molecular level, the surface reactions during the Mn(EtCp)<sub>2</sub> exposure were given by Equation (2).<sup>35</sup> Here \* refers to surface reactive species.



Mn(EtCp)<sub>2</sub> can react with surface hydroxyl groups and releases a complex of protons (possibly attached to H<sub>2</sub>O molecules) and EtCp anions as a product, i.e. H<sup>+</sup>[EtCp]<sup>-</sup>. The subsequent surface reactions during the H<sub>2</sub>O exposure are given by Equations (3) and (4).<sup>35</sup>



H<sub>2</sub>O can react with a surface MnEtCp\* to result in a hydroxyl-terminated surface, after which MnO<sub>x</sub> will complete its deposition on the substrate. At the first cycle, Mn(EtCp)<sub>2</sub> will react with surface hydroxyl group on the NiFe-LDH substrate to produce a certain number of nucleation sites. In the following ALD cycles, the growth of MnO<sub>x</sub> was continued on these MnO<sub>x</sub> sites to generate partially covered structures of MnO<sub>x</sub> nano-islands on LDH nanosheet surfaces, as indicated in Equation (4). Unreacted precursor molecules, along with volatile products, were removed in a continuous flow of inert Ar gas. The crystal structures of the as-prepared samples with varying ALD MnO<sub>x</sub> cycles (from 5 to 50) were characterized by XRD, as shown in Fig. 1. Three evident diffraction peaks, located at 44.3°, 51.8°, and 76.5°, corresponded to the (111), (200), and (220) crystal planes of Ni foam substrates (PDF No. 70-0989), respectively. Prior to the ALD process, the NiFe-LDH samples generated XRD patterns with diffraction peaks at 11.35°, 22.74°, 34.41°, 38.77°, and 59.98°, which were assigned to the (003), (006), (012), (015), and (110) crystal planes of layered NiFe-LDH.<sup>38</sup> The peak intensity of LDH was relatively weak, which is mainly caused by the overshadowing effect of Ni foam substrates.<sup>39</sup> After the ALD process, no additional diffraction peaks were introduced. In fact, the intensity of most NiFe-LDH peaks decreased slightly because the surface-deposited amorphous MnO<sub>x</sub> reduced the ordering of the crystal planes of NiFe-LDH other than (006) planes. By analyzing all the diffraction peaks from NiFe-LDH with the varying ALD MnO<sub>x</sub> cycles, it was concluded that the predominant NiFe-LDH phase was either low crystallinity or amorphous. Regarding the structure of MnO<sub>x</sub> surface modification, few layers of Mn-O octahedral clusters that were aggregated in a flat nano-island shape should be good representation: these nano-islands covered the surfaces of

NiFe-LDH nanosheets uniformly throughout the electrode surfaces, and were in contact with liquid electrolytes during catalyst operation.

The OER performance of the as-grown NiFe-LDH and MnO<sub>x</sub>/NiFe-LDH was evaluated in a 1 M KOH (aq) electrolyte by cyclic voltammetry. As shown in Fig. 2a, the overpotentials at a current density of 10 mA cm<sup>-2</sup> were measured to be 216, 192, 174, 178, and 199 mV for the 0, 5, 10, 20, and 50 cycles of ALD MnO<sub>x</sub>, respectively. The standard deviations of the measured overpotentials were ±10 mV. In comparison to original NiFe-LDH, the OER activity can be enhanced by ALD MnO<sub>x</sub> modification in varying degrees but with slight differences. Among them, the 10-cycle of ALD MnO<sub>x</sub>/LDH exhibited the best OER performance, and its pre-catalytic redox wave showed the largest anodic shift which is consistent with the strong electronic interactions reported for Co-Fe systems.<sup>40</sup> To achieve a catalytic current density of 50 mA cm<sup>-2</sup>, an overpotential of 283 mV was only needed for the 10-cycle of MnO<sub>x</sub>/LDH, which is much lower than that of original LDH (357 mV). The NiFeMn-LDH electrocatalysts were nanosheet structures consisting of homogeneously distributed Ni, Fe, and Mn elements without over-coated MnO<sub>x</sub> islands. They also showed improved OER activity with the introduction of Mn into the LDH nanomaterials. However, their activity was lower than that of ALD MnO<sub>x</sub>-modified samples that are featured with the engineered MnO<sub>x</sub>/NiFe-LDH interfaces. Additionally, we compared the electrochemical kinetics of the ALD samples with the original NiFe-LDH in a Tafel plot as shown in Fig. 2b. The Tafel slope of 10-cycle of MnO<sub>x</sub>/NiFe-LDH sample (48 mV dec<sup>-1</sup>) was smaller than that of original NiFe-LDH (65 mV dec<sup>-1</sup>) without MnO<sub>x</sub> modification. This comparison illustrated that the MnO<sub>x</sub>-modified nanocomposites favored faster kinetics at a reduced Tafel slope and possibly with a shift in the catalytic

mechanism. The Tafel slope provides important information about the rate determining step (RDS) of four-electron/four-proton OER reactions. The corresponding Tafel slope of the second-electron-transfer limited mechanism would be between  $70 \text{ mV dec}^{-1}$  and  $30 \text{ mV dec}^{-1}$  if the second electron-transfer step of chemical O-O coupling and the resulting  $\ast\text{OOH}$  formation was the RDS,<sup>41</sup> whereas the Tafel slope of the third-electron-transfer limited mechanism would be  $30 \text{ mV dec}^{-1}$ . Hence, the change in the Tafel slope from 65 to  $48 \text{ mV dec}^{-1}$  for the  $\text{MnO}_x$  modified sample suggested a changing trend for the RDS from predominately the second electron-transfer step to the third electron-transfer step of  $\ast\text{OOH}$  deprotonation and  $\text{O}_2$  release upon  $\text{MnO}_x$  modification.<sup>41</sup> This mechanistic shift is a definitive sign for the ALD modifications to improve electrocatalytic activity. Therefore, 10-cycle of ALD  $\text{MnO}_x/\text{NiFe-LDH}$  was considered as the representative OER electrode for further materials characterization and spectroscopic analysis.

Fig. 3 shows SEM images of the 10-cycle of ALD  $\text{MnO}_x$  grown on top of the NiFe-LDH nanosheets. The nanosheet structure of modified NiFe-LDH (Fig. 3a and 3b) was well-retained from its original morphology (Fig. 3c and 3d). For such highly non-uniform and non-planar surfaces of NiFe-LDH, the exceptional conformality by the ALD coating is well demonstrated: nanometer-scale  $\text{MnO}_x$  islands were observed to cover the surfaces of LDH sheets, as shown in Fig. 3b, but not to replace surface Ni or Fe cations. Furthermore, TEM was employed for characterizing the nanoscale heterostructured interfaces, for example, by using fragments of the  $\text{MnO}_x/\text{LDH}$  samples (exfoliated from the electrode carefully) (shown in Fig. 4a). The high-resolution TEM images exhibited lattice fringes with an interplanar spacing of 0.25 nm corresponding to the spacing of (012) crystal planes of NiFe-LDH.<sup>16</sup> Amorphous  $\text{MnO}_x$  nano-islands were uniformly

grown onto the nanosheets (Fig. 4b). To further evaluate the morphology and the composition of the as-fabricated electrode materials, a HAADF-STEM mode with energy-dispersive X-ray spectroscopy (EDX) was employed. The areal average of EDX composition mapping gave 8% Mn in atomic percentage on the NiFe-LDH sample surface (Fig. 4c). As shown in the EDX elemental mapping (Fig. 4d), the majority of Ni, Fe, and O elements were uniformly distributed within the nanosheets, while islands of Mn elements were distributed over the NiFe-LDH surface randomly but with a homogenous distribution. This observation indicated that the nano-interfaces of  $\text{MnO}_x/\text{NiFe-LDH}$  heterostructures were successfully constructed. The heterostructured  $\text{MnO}_x/\text{NiFe-LDH}$  nano-interfaces created a large amount of edge sites, which are identified as one of the major reasons for boosting OER activity of the electrodes (see discussion below). The partially covered LDH catalysts consist of exposed edge sites at  $\text{MnO}_x/\text{NiFe-LDH}$  nano-interfaces, which operated synergistically for OER, side-by-side with the original and uncovered NiFe-LDH catalytic sites.

To understand the electronic interaction between  $\text{MnO}_x$  and NiFe-LDH, the elemental composition and valance states of the 10-cycle ALD  $\text{MnO}_x/\text{NiFe-LDH}$  sample were investigated by XPS. The XPS survey spectrum confirmed the presence of Ni, Fe, O, and Mn on the sample surface (Fig. S4). The XPS spectrum of Mn  $2p_{3/2}$  core-level photoemission was deconvoluted by six Gaussian peaks following our published work as shown in Fig. 5a, where the binding energies of the respective peaks were listed in Table S1.<sup>34</sup> In order to determine the valance state of Mn, pure ALD  $\text{MnO}_x$  was used for comparison. The fitting results indicated that Mn in  $\text{MnO}_x$  was predominantly +2 in valency for both ALD  $\text{MnO}_x$  and  $\text{MnO}_x/\text{LDH}$  nanocomposites. Furthermore, when  $\text{MnO}_x$

islands were deposited on NiFe-LDH, a small positive shift in the position of Mn  $2p_{3/2}$  signal intensity maxima were observed (from 641.9 to 642.0 eV) and the fitted peak (peak 1 labelled by a black arrow) at a binding energy of 640.2 eV increased in intensity as compared to ALD  $MnO_x$  (Fig. 5a). Both observations indicated that  $MnO_x$  received electrons and became electron-rich. In other words,  $MnO_x$  filled its empty states showing a raised Fermi level as evident by a slight increase of Mn  $2p_{3/2}$  core-level binding energies.

Accordingly, we would expect a depletion of surface electrons for NiFe-LDH nanosheets, which would be evident by a decrease in binding energies for Ni  $2p_{3/2}$  and Fe  $2p_{3/2}$  XPS core-level spectra after  $MnO_x$  modification. In other words, Ni or Fe core-level binding energy, i.e. the energy-level difference spanning from the NiFe-LDH Fermi level to the core level of Ni or Fe cations, would be reduced. A similar energy-level analysis by photoelectron spectroscopy was described previously.<sup>42</sup> The XPS spectra of Ni  $2p_{3/2}$  and Fe  $2p_{3/2}$  photoemission were curve-fitted as shown in Fig. 5b and 5c. Their binding energies of 856.0 and 713.0 eV for  $MnO_x$ /NiFe-LDH composite were attributed to the  $Ni^{2+}$  and  $Fe^{3+}$ , respectively.<sup>13, 43</sup> These valance states are in good agreement with those measured for the original NiFe-LDH. The Fermi level of NiFe-LDH nanosheets were found to be modified by  $MnO_x$  overlayers: the binding energy of Ni  $2p_{2/3}$  and Fe  $2p_{2/3}$  peak positions in  $MnO_x$ -modified NiFe-LDH (856.0 eV and 713.0 eV) was lower than those of the original NiFe-LDH (856.8 eV and 715.0 eV). This electron depletion at NiFe-LDH surfaces was indicative of the covalent coordination and electronic interaction between NiFe-LDH nanosheets and ALD-overgrown  $MnO_x$ . Therefore, it confirmed the tuning of NiFe-LDH electronic properties by anchoring  $MnO_x$  nano-islands on catalyst

surfaces.

To further understand the electrochemical performance of MnO<sub>x</sub>/NiFe-LDH nanocomposites, turnover frequency (TOF), electrochemical impedance, Faradaic efficiency, and long-term durability were quantified. The molar amount of metal elements in these samples were determined by ICP-MS as listed in Table S3. Based on Equation 1, the lower limit of TOFs for MnO<sub>x</sub>/LDH and NiFe-LDH at 300 mV overpotentials are 0.0066 and 0.0043 s<sup>-1</sup> as shown in Table S4, demonstrating the intrinsic OER activity of MnO<sub>x</sub>/LDH active sites is better than the original NiFe-LDH without modification. The EIS analysis indicated that MnO<sub>x</sub>/LDH nanocomposites had a lower charge-transfer resistance ( $R_{ct}$ , 5.89  $\Omega$ ) than that of original LDH (8.13  $\Omega$ ) as shown in Fig. S3, suggesting a faster electron transfer process during OER. Moreover, the quantity of oxygen accumulated at 10 mA cm<sup>-2</sup> based on MnO<sub>x</sub>/NiFe-LDH nanocomposites matched with the calculated amount for OER assuming a Faradaic efficiency of ~100% as shown in Fig. 5d. The long-term performance stability during the OER is important for practical applications. Chronopotentiometry measurements showed excellent stability of NiFe-LDH as the catalysts operated at a constant current density of 10 mA cm<sup>-2</sup> for 10 h, comparable to that of original NiFe-LDH.<sup>8, 13</sup> Only 6 mV increase of the overpotential was observed during 10 h operation, which affirms the structural and functional stability of covalent bonding between ALD MnO<sub>x</sub> and NiFe-LDH nanosheets. According to the SEM image of the 10-cycle ALD MnO<sub>x</sub>/NiFe-LDH electrode after long-term electrocatalysis (Fig. S5), the nanosheet morphology was maintained, suggesting excellent structural stability. Additionally, the composition analysis for the electrode material after 10 h stability testing as determined by ICP-MS (Table S3) revealed that the

ratios of Ni/Fe/Mn metal elements or the Mn composition in the  $\text{MnO}_x/\text{NiFe-LDH}$  sample were close to those values before long-term electrocatalysis. These results indicate that the active site structures of  $\text{MnO}_x$  were well preserved after 10 h operation. Furthermore, XPS was also employed to evaluate the chemical stability of the  $\text{MnO}_x/\text{LDH}$  surface after the 10 h operation. The valence states of  $\text{MnO}_x$  nano-islands after OER showed no obvious change (Fig. 4a), which indicated the chemical stability of the  $\text{Mn}^{2+}$  cations during long-term OER operation. This is also consistent with the reported electrochemical performance stability.

As for the mechanism of improved OER activity, both structural effects and electronic tuning of 3D  $\text{MnO}_x/\text{NiFe-LDH}$  nano-interfaces are considered to be at work. Ab initio calculations and in-situ spectroscopic measurements reported that the original NiFe-LDH systems featured cooperation between Fe(IV) (which first stabilizes O radicals) and Ni(IV) (which then catalyzes chemical O-O coupling).<sup>15, 41</sup> Exchange interactions between di-valent metal centres, e.g. neighboring Ni and Fe cations, was recently considered, which suggests the delocalization of electron spins from high spin  $\text{Fe}^{4+}$  centres reduces the free energy cost for the O-O coupling RDS. After  $\text{MnO}_x$  deposition and modification, the spin correlation between  $\text{Mn(II)O}_x$  with a high spin  $d^5$  configuration and Ni-Fe centres may further reduce the activation barrier for the O-O coupling RDS, which is consistent with the reduced Tafel slope from  $65 \text{ mV dec}^{-1}$  to  $48 \text{ mV dec}^{-1}$ . In this case, atomically precise  $\text{MnO}_x$  modification created a large amount of active edge sites at  $\text{MnO}_x/\text{NiFe-LDH}$  nano-interfaces. The enhancement of  $\text{MnO}_x$ -induced edge sites outperforms the original Ni and Fe active sites covered by  $\text{MnO}_x$  nano-islands. The  $\text{MnO}_x$  nano-islands induced electronic tuning to original NiFe-LDH



nanosheets. Furthermore, the structural environment at newly introduced edge sites by  $\text{MnO}_x/\text{NiFe-LDH}$  nanocomposites could stabilize reaction intermediates and enhance the oxidative activity of NiFe-LDH.<sup>44</sup> Therefore, the above analysis clearly suggested the advantage of both structural and electronic tuning via  $\text{MnO}_x/\text{LDH}$  nanocomposites for boosting the OER activity. As the structure and valence state of  $\text{MnO}_x$  nano-islands perseverated as characterized after the stability test, these 3D nano-interfaces promise long-lasting improvements to the OER activity.

#### 4. Conclusions

In summary, the heterostructures of  $\text{MnO}_x/\text{NiFe-LDH}$  nano-composites were successfully fabricated and finely tuned by few-cycle atomic layer deposition (ALD) over hydrothermally grown NiFe-LDH oxygen evolving catalysts. The  $\text{MnO}_x$  nano-islands that were uniformly anchored on the LDH support created a high density of functional nano-interfaces. The 3D engineering of  $\text{MnO}_x/\text{LDH}$  nano-interfaces resulted in electronic tuning of NiFe-LDH catalytic sites on the nanosheets, and additionally introduced new active sites at edges of  $\text{MnO}_x$  nano-islands that outperform those on the original NiFe-LDH. The optimized combination of 10-cycle ALD  $\text{MnO}_x/\text{NiFe-LDH}$  nanosheets showed the highest OER activity, affording a current density of  $10 \text{ mA cm}^{-2}$  at a small overpotential of 174 mV, a Tafel slope as small as  $48 \text{ mV dec}^{-1}$ , and 10-hour stability in alkaline media. The presented surface modification not only provides a promising pathway towards efficient non-precious metal oxide OER electrocatalysts, but also offers insights into the construction of new types of electrocatalytic active sites, such as ALD-grown 3D nano-interfaces, on energy converting materials.

## Conflicts of interest

There are no conflicts to declare.

## Acknowledgements

Y. Xue acknowledges the financial support of the University of Chinese Academy of Sciences (UCAS[2015]37) Joint PhD Training Program. S. Zheng acknowledges the funding support from National Natural Science Foundation of China (No. 51774261). S. Hu thanks the grant support from the Office of Naval Research under the award number N00014-18-1-2576. The authors would like to thank Dr. Min Li at Yale's Materials Characterization Core (MCC) for his invaluable help with XRD, SEM and XPS and Dr. Michael Rooks at the Yale Institute for Nanoscience and Quantum Engineering (YINQE) for the TEM characterization.

## References

1. J. Luo, J. H. Im, M. T. Mayer, M. Schreier, M. K. Nazeeruddin, N. G. Park, S. D. Tilley, H. J. Fan and M. Gratzel, *Science*, 2014, **345**, 1593-1596.
2. Q. Li, D. Wang, C. Han, X. Ma, Q. Lu, Z. Xing and X. Yang, *J. Mater. Chem. A*, 2018, **6**, 8233-8237.
3. B. M. Hunter, H. B. Gray and A. M. Muller, *Chem. Rev.*, 2016, **116**, 14120-14136.
4. L. Yu, J. F. Yang, B. Y. Guan, Y. Lu and X. W. D. Lou, *Angew. Chem. Int. Ed.*, 2018, **57**, 172-176.

5. J. Tian, J. Chen, J. Liu, Q. Tian and P. Chen, *Nano Energy*, 2018, **48**, 284-291.
6. Z. W. Seh, J. Kibsgaard, C. F. Dickens, I. Chorkendorff, J. K. Nørskov and T. F. Jaramillo, *Science*, 2017, **355**.
7. N. T. Suen, S. F. Hung, Q. Quan, N. Zhang, Y. J. Xu and H. M. Chen, *Chem. Soc. Rev.*, 2017, **46**, 337-365.
8. S. Jung, C. C. L. McCrory, I. M. Ferrer, J. C. Peters and T. F. Jaramillo, *J. Mater. Chem. A*, 2016, **4**, 3068-3076.
9. J. Nai, Y. Lu and X.-Y. Yu, *J. Mater. Chem. A*, 2018, DOI: 10.1039/c8ta02334d.
10. X. Zhao, F. Li, R. Wang, J.-M. Seo, H.-J. Choi, S.-M. Jung, J. Mahmood, I.-Y. Jeon and J.-B. Baek, *Adv. Funct. Mater.*, 2017, **27**, 1605717.
11. Y. Zhou, S. Sun, J. Song, S. Xi, B. Chen, Y. Du, A. C. Fisher, F. Cheng, X. Wang, H. Zhang and Z. J. Xu, *Adv Mater*, 2018, **30**, e1802912.
12. W. Xu, F. Lyu, Y. Bai, A. Gao, J. Feng, Z. Cai and Y. Yin, *Nano Energy*, 2018, **43**, 110-116.
13. Z. Lu, W. Xu, W. Zhu, Q. Yang, X. Lei, J. Liu, Y. Li, X. Sun and X. Duan, *Chem. Commun.*, 2014, **50**, 6479-6482.
14. H. Yin and Z. Tang, *Chem. Soc. Rev.*, 2016, **45**, 4873-4891.
15. B. M. Hunter, N. B. Thompson, A. M. Müller, G. R. Rossman, M. G. Hill, J. R. Winkler and H. B. Gray, *Joule*, 2018, **2**, 747-763.
16. M. Gong, Y. Li, H. Wang, Y. Liang, J. Z. Wu, J. Zhou, J. Wang, T. Regier, F. Wei and H. Dai, *J. Am. Chem. Soc.*, 2013, **135**, 8452-8455.
17. D. Zhou, X. Xiong, Z. Cai, N. Han, Y. Jia, Q. Xie, X. Duan, T. Xie, X. Zheng, X. Sun and X. Duan, *Small*, 2018, **2**, 1800083.

18. Q. Wang and D. O'Hare, *Chem. Rev.*, 2012, **112**, 4124-4155.
19. K. Jin, H. Seo, T. Hayashi, M. Balamurugan, D. Jeong, Y. K. Go, J. S. Hong, K. H. Cho, H. Kakizaki, N. Bonnet-Mercier, M. G. Kim, S. H. Kim, R. Nakamura and K. T. Nam, *J. Am. Chem. Soc.*, 2017, **139**, 2277-2285.
20. K. R. Yang, A. J. Matula, G. Kwon, J. Hong, S. W. Sheehan, J. M. Thomsen, G. W. Brudvig, R. H. Crabtree, D. M. Tiede, L. X. Chen and V. S. Batista, *J. Am. Chem. Soc.*, 2016, **138**, 5511-5514.
21. N. C. Strandwitz, D. J. Comstock, R. L. Grimm, A. C. Nichols-Nielander, J. Elam and N. S. Lewis, *J. Phy. Chem. C*, 2013, **117**, 4931-4936.
22. L. C. Seitz, T. J. Hersbach, D. Nordlund and T. F. Jaramillo, *J. Phys. Chem. Lett.*, 2015, **6**, 4178-4183.
23. M. Huynh, C. Shi, S. J. Billinge and D. G. Nocera, *J. Am. Chem. Soc.*, 2015, **137**, 14887-14904.
24. Z. Morgan Chan, D. A. Kitchaev, J. Nelson Weker, C. Schnedermann, K. Lim, G. Ceder, W. Tumas, M. F. Toney and D. G. Nocera, *Proc. Natl. Acad. Sci. USA*, 2018, **115**, E5261-E5268.
25. T. Takashima, K. Hashimoto and R. Nakamura, *J. Am. Chem. Soc.*, 2012, **134**, 1519-1527.
26. K. Jin, A. Chu, J. Park, D. Jeong, S. E. Jerng, U. Sim, H. Y. Jeong, C. W. Lee, Y. S. Park, K. D. Yang, G. Kumar Pradhan, D. Kim, N. E. Sung, S. Hee Kim and K. T. Nam, *Sci. Rep.*, 2015, **5**, 10279.
27. C. Bae, T. A. Ho, H. Kim, S. Lee, S. Lim, M. Kim, H. Yoo, J. M. Montero-Moreno, J. H. Park and H. Shin, *Sci. Adv.*, 2017, **3**, e1602215.

28. M. Liu, X. Li, S. K. Karuturi, A. I. Tok and H. J. Fan, *Nanoscale*, 2012, **4**, 1522-1528.
29. S. Hu, M. R. Shaner, J. A. Beardslee, M. Lichterman, B. S. Brunshwig and N. S. Lewis, *Science*, 2014, **344**, 1005-1009.
30. A. C. Bronneberg, C. Höhn and R. van de Krol, *J. Phy. Chem. C*, 2017, **121**, 5531-5538.
31. T. Moehl, J. Suh, L. Severy, R. Wick-Joliat and S. D. Tilley, *ACS Appl. Mater. Inter.*, 2017, **9**, 43614-43622.
32. L. Chen, J. Yang, S. Klaus, L. J. Lee, R. Woods-Robinson, J. Ma, Y. Lum, J. K. Cooper, F. M. Toma, L. W. Wang, I. D. Sharp, A. T. Bell and J. W. Ager, *J. Am. Chem. Soc.*, 2015, **137**, 9595-9603.
33. T. Yao, R. Chen, J. Li, J. Han, W. Qin, H. Wang, J. Shi, F. Fan and C. Li, *J. Am. Chem. Soc.*, 2016, **138**, 13664-13672.
34. G. Siddiqi, Z. Luo, Y. Xie, Z. Pan, Q. Zhu, J. A. Röhr, J. J. Cha and S. Hu, *ACS Appl. Mater. Inter.*, 2018, **10**, 18805-18815.
35. B. B. Burton, F. H. Fabreguette and S. M. George, *Thin Solid Films*, 2009, **517**, 5658-5665.
36. F. Lyu, Y. Bai, Z. Li, W. Xu, Q. Wang, J. Mao, L. Wang, X. Zhang and Y. Yin, *Adv. Funct. Mater.*, 2017, **27**, 1702324.
37. M. B. Stevens, L. J. Enman, A. S. Batchellor, M. R. Cosby, A. E. Vise, C. D. M. Trang and S. W. Boettcher, *Chemistry of Materials*, 2016, **29**, 120-140.
38. H. Xu, B. Wang, C. Shan, P. Xi, W. Liu and Y. Tang, *ACS Appl. Mater. Inter.*, 2018, **10**, 6336-6345.

39. F. S. Zhang, J. W. Wang, J. Luo, R. R. Liu, Z. M. Zhang, C. T. He and T. B. Lu, *Chem. Sci.*, 2018, **9**, 1375-1384.
40. M. S. Burke, M. G. Kast, L. Trotochaud, A. M. Smith and S. W. Boettcher, *J. Am. Chem. Soc.*, 2015, **137**, 3638-3648.
41. H. Xiao, H. Shin and W. A. Goddard, *Proc. Natl. Acad. Sci. USA*, 2018, **115**, 5872-5877.
42. S. Hu, M. H. Richter, M. F. Lichterman, J. Beardslee, T. Mayer, B. S. Brunschwig and N. S. Lewis, *J. Phy. Chem. C*, 2016, **120**, 3117-3129.
43. J. Hu, C. Zhang, L. Jiang, H. Lin, Y. An, D. Zhou, M. K. H. Leung and S. Yang, *Joule*, 2017, **1**, 383-393.
44. J. K. Nørskov, J. Rossmeisl, A. Logadottir, L. Lindqvist, J. R. Kitchin, T. Bligaard and H. Jónsson, *J. Phy. Chem. B*, 2004, **108**, 17886-17892.